Antiferromagnetic-ferromagnetic homostructures with Dirac magnons in the van der Waals magnet CrI_3

John A. Schneeloch,[1] Luke Daemen,[2] and Despina Louca[1,*]
[1]*Department of Physics, University of Virginia, Charlottesville, Virginia 22904, USA*
[2]*Neutron Scattering Division, Oak Ridge National Laboratory, Oak Ridge, Tennessee 37831, USA*

(Received 11 July 2023; revised 1 November 2023; accepted 11 December 2023; published 10 January 2024)

The Dirac magnon system CrI_3 with a honeycomb lattice is a potential host of topological edge magnons. It ideally orders ferromagnetically (FM) ($T_c = 61$ K) on cooling from a monoclinic (M) to a rhombohedral (R) phase, but antiferromagnetic (AFM) order has been detected in nanometer thin flakes, attributed to M-type layer stacking. There remains confusion, however, as to the extent to which such behavior is present in bulk samples. Using a powder sample in which the sliding transition to the R phase was largely inhibited (2:1 M:R ratio), clear evidence for M-type AFM order ($T_N \sim 50$ K) coexisting with R-type FM order is observed in the bulk. From inelastic neutron scattering, a lower magnon energy is observed compared to the R phase, consistent with smaller interlayer interactions expected in the M phase. While a gap at the Dirac points has been reported in the R phase, the gap is clearly observed even when the majority is M type, as in our sample, suggesting that the same nontrivial magnon topology of the R phase is present in the M phase as well.

DOI: 10.1103/PhysRevB.109.024409

I. INTRODUCTION

The discovery of giant magnetoresistance, built on alternating layers of ferromagnetic (FM) and antiferromagnetic (AFM) magnetic order [1,2], has revolutionized device concepts based on heterostructures. Nowadays, the exfoliation of single atomic layers from bulk van der Waals (vdW) crystals [3] is leading a similar revolution, enabling new discoveries. In twisted graphene, for example [4], the observation of superconductivity is a demonstration of what single-layer manipulation can do. More recently, multiple stacking possibilities in vdW crystals have been shown to lead to markedly different behaviors. For instance, transitions from nontrivial to topological band structures have been observed in the Weyl semimetal $MoTe_2$ from the $1T'$ (monoclinic) to T_d (orthorhombic) phases [5,6] or from a weak to a strong topological insulator in Bi_4I_4 [7,8]. The magnetic behavior may change with the stacking as well, such as the roughly tenfold increase in the interlayer magnetic coupling reported for $CrCl_3$ when the layer stacking present at high temperatures is preserved at low temperatures [9,10].

CrI_3 consists of layers of honeycomb lattices of Cr^{3+} ions with $S = 3/2$ spins sandwiched between two triangular lattices of I^- ions. The I^- ions of one layer sit in the middle of the triangles of the neighboring I^- lattice [Fig. 1(a)]. Bulk crystals become FM below $T_C = 61$ K, with the spins oriented out of plane [11]. In thin flakes, on the other hand, the spin alignment is AFM with the spin direction (pointing out of plane) alternating layer by layer [12], as deduced from techniques such as the magneto-optical Kerr effect [12,13], magnetic circular dichroism [14–16], magnetic force microscopy [17], scanning magnetometry [18], and tunneling magnetoresistance [13,19–21].

The AFM order in flakes of CrI_3 arises from monoclinic $C2/m$ (M-type) stacking that is present because of the arrested transition to the rhombohedral $R\bar{3}$ (R-type) stacking [13,16,22–27]. There are two sets of symmetry-equivalent stacking possibilities, with three M-type and two R-type stacking options [Figs. 1(c) and 1(d)]. In principle, the M-type stacking disappears in bulk CrI_3 on cooling during the layer-sliding transition from the M phase to the R phase below ~180 K [11,28].

However, even in single crystals, the M → R transition may occur over a broad temperature range or be inhibited entirely (as can be seen in our single-crystal x-ray diffraction measurements in the Supplemental Material, Fig. S1 [29]), and the process may proceed differently in subsequent thermal cycles [11]. The thickness of the crystals is also an important factor in inhibiting the transition, as shown from split vibrational modes, observed in the Raman spectroscopy of a thin flake, that fail to merge (as expected for $R\bar{3}$) down to at least 10 K [30]. The dependence on thickness of layer-sliding transitions has also been observed in $MoTe_2$, where the transition temperature range broadens (or is inhibited entirely) for crystals with a thickness below ~120 nm [31,32].) Surface layers of CrI_3 crystals have also been reported to exhibit AFM ordering, presumably from M-type stacking [17,33,34]. At the same time, several bulk measurements hint at the presence of magnetic ordering beyond the reported ferromagnetism. Anomalies near ~50 K in magnetic susceptibility have been reported in bulk crystals [11,13,35,36]. Additionally, from muon spin resonance (μSR) measurements, a second magnetic component has been reported [37]; the authors of this study declined to identify AFM ordering as the source of this component, understandably given the lack of direct evidence

*louca@virginia.edu

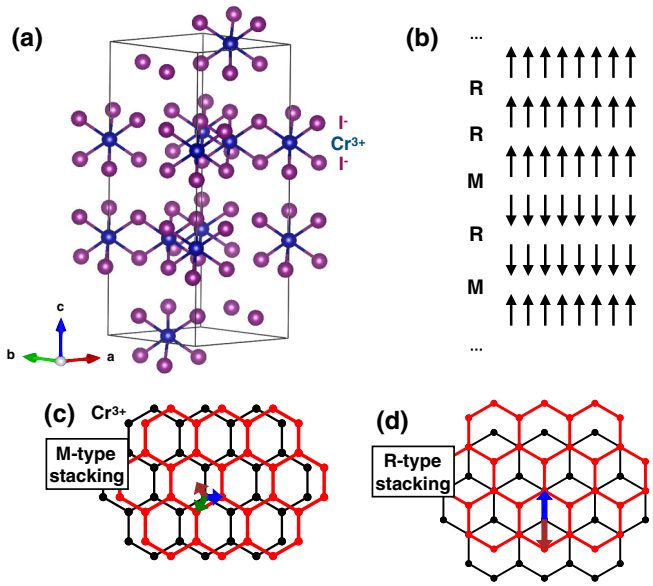

FIG. 1. (a) Crystal structure of the $R\bar{3}$ phase of CrI_3. (b) A schematic showing how the spin direction would change, layer by layer, in M- and R-type stacking, with spin flips accompanying M-type stacking. (c), (d) Illustration of (c) M-type and (d) R-type layer stacking. The honeycomb lattice represents the placement of the Cr^{3+} ions, with the red lattice above the black showing one possible stacking option; the displacements for the full set of stacking options are shown as arrows.

for a correspondence between AFM ordering and M-type stacking boundaries in bulk CrI_3, but indicating the need for such an investigation.

CrI_3 is also a candidate material for observing topological magnons [38]. CrI_3 has been probed via inelastic neutron scattering in several recent studies [39–42], in which the spin waves were described in terms of a dispersion reminiscent of the electronic band structure of graphene, but with the Dzyaloshinskii-Moriya (DM) interaction reportedly opening a gap of 2.8 meV at the Dirac points [41].

With neutron scattering, we elucidate the dual magnetic nature of CrI_3 by providing direct evidence of M-type stacking with AFM order that alternates with R-type stacking with FM order in bulk samples. Elastic neutron scattering measurements on ground CrI_3 powder show magnetic elastic intensity that is consistent with a model where the spin direction flips across M-type interlayer boundaries. Thus, control of the M-to-R layering can provide a homostructure with AFM-to-FM order. The AFM ordering vanishes above ∼50–55 K, while the FM ordering persists to ∼60 K. From inelastic neutron scattering, a $\lesssim 1$ meV decrease in energy relative to the reported single-crystal dispersion is observed. A gap is present at the Dirac node, suggesting its presence (and the possibility of topological magnons) in the M phase as well as the R phase.

II. EXPERIMENTAL DETAILS

Stoichiometric amounts of Cr and I powders were sealed into ampoules. The ampoules were heated at 100 °C/h to 650 °C, then kept there for three days before cooling to room temperature. The resulting powder, about 5 g, was ground for several minutes in a mortar and pestle in an argon glove bag prior to the neutron experiment. For the magnetic susceptibility measurements, the powder was pressed into a pellet under argon atmosphere.

Neutron scattering measurements were carried out on the VISION instrument at the Spallation Neutron Source of Oak Ridge National Laboratory. VISION is an indirect-geometry time-of-flight spectrometer. The final neutron energy was fixed at 3.5 meV. Inelastic data were taken on two detector banks at scattering angles of 45° and 135°, corresponding to low-Q and high-Q momentum transfer neutron scattering trajectories; all the data discussed in this work were taken on the low-Q detector banks, where the magnetic intensity was stronger and the phonon intensity weaker.

Simultaneously with the inelastic data, elastic data were taken on six detector banks at a 90° scattering angle. The elastic data were generally averaged over the six banks, except for refinement, which was done with bank no. 6. The CrI_3 sample was cooled to 5 K, warmed to 140 K, cooled to 15 K, and warmed to 275 K; the data shown are from the warming portions (5–140 K and 175–275 K). Positions in reciprocal space that are labeled $(hkl)_R$ or $(hkl)_M$ correspond to $R\bar{3}$- or $C2/m$-phase reciprocal space coordinates, respectively.

Magnetization measurements were performed in a Quantum Design Physical Property Measurement System (PPMS) equipped with a Vibrating Sample Magnetometer.

III. RESULTS

A. Elastic neutron scattering

Neutron scattering data on a sample of CrI_3 powder (which had been ground for a few minutes in a mortar and pestle) were taken on the VISION instrument at Oak Ridge National Laboratory, which collects elastic and inelastic data on two separate sets of detectors. The elastic neutron scattering data collected at 5 K are shown in Fig. 2(a) as a function of d-spacing, where $d = \frac{2\pi}{Q}$ and Q is the momentum transfer. Also shown are the simulated intensities for the $R\bar{3}$ and $C2/m$ phases and a Cr_2O_3 impurity phase. (Interestingly, CrI_3 lacks the clear in-plane negative thermal expansion of $CrBr_3$ and $CrCl_3$; see Supplemental Material, Sec. II [29].) As shown in Fig. 2(b), there is minimal change in the intensity on warming from 70 to 200 K. Only localized changes are seen from 200 to 275 K [Fig. 2(c)], in the form of the expected shrinking of $R\bar{3}$ peaks [such as $(113)_R$] and growing intensity of $C2/m$ peaks [such as $(131)_M$]. Overall, though, it is clear that the intensity in the $2.7 \leqslant d \leqslant 3.5$ Å range [highlighted in green in Fig. 2(a)] cannot be represented by the ordered $R\bar{3}$ and $C2/m$ phases alone, and that substantial diffuse scattering is present arising from disordered R- and M-type layer stacking.

The percentages of M- and R-type stacking was estimated from Rietveld refinement at low d/high Q, where the intensity of a randomly stacked R/M mixture can be approximated by a linear combination of intensity arising from the two phases ($R\bar{3}$ and $C2/m$; see Supplemental Material, Sec. III [29]). At 5 K, the sample consists of about 63% M-type and 37% R-type stacking. A Cr_2O_3 second phase is present as well at about 5 wt%. There are additional, likely magnetic, peaks near

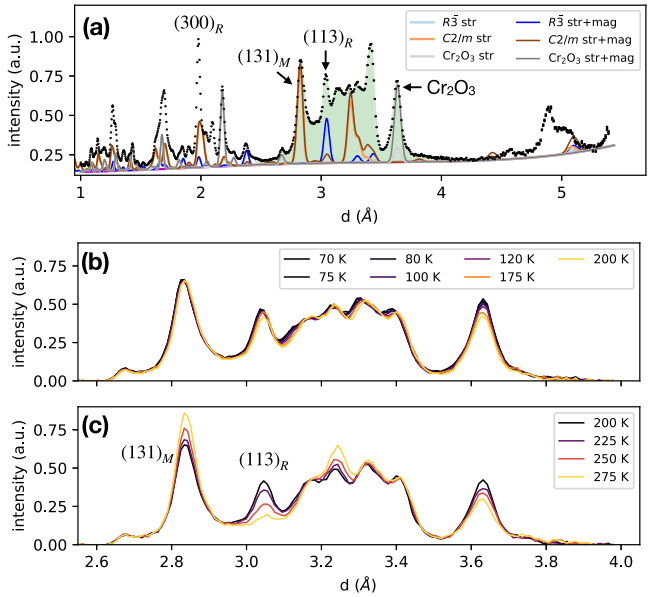

FIG. 2. (a) Data at 5 K (black points), along with curves of simulated intensity for the $R\bar{3}$ and $C2/m$ CrI_3 phases and the Cr_2O_3 impurity phase, both for the nuclear ("str") intensity alone and with the magnetic intensity (in the M-AFM model) included. The region of focus ($2.45 \leqslant d \leqslant 3.9$ Å) is shaded. (b), (c) Elastic intensity within (c) 70 to 200 K and (d) 200 to 275 K, with a linear background subtracted to account for its temperature dependence. Error bars in (a) are often smaller than the marker size; error bars are omitted in (b) and (c) for clarity, but uncertainty is commensurate with scatter.

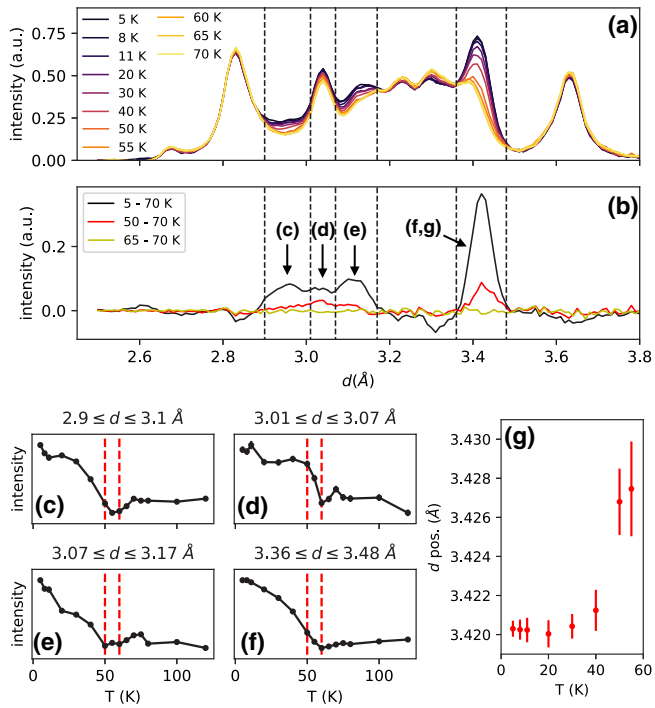

FIG. 3. (a) Elastic scattering intensity vs layer spacing d. A linear background was subtracted for each temperature. (b) Intensity with the 70 K data subtracted for $T = 5$, 50, and 65 K, to show the magnetic contribution. Error bars are omitted in (a) and (b) for clarity, but uncertainty is commensurate with scatter. [(c)–(f)] Integrated intensity of the raw data within the regions labeled in (b), plotted vs temperature; red dashed lines show 50 and 60 K. (g) Fitted position vs temperature of the peak in (b) near $d = 3.43$ Å.

$d = 5.0$ Å that arise below ~20 K, along with low-energy ($\hbar\omega < 4$ meV) spin-wave intensity (see Supplemental Material, Sec. IV [29]). We have not identified the source of these peaks, but they do not affect our results since they are only present at low temperature.

In Fig. 3(a), the temperature dependence of the elastic intensity is shown from 5 to 70 K in the range of $2.5 \leqslant d \leqslant 3.8$ Å. Since the intensity does not change from 70 to 200 K, we use the 70 K data as a background to subtract from the 5, 50, and 60 K data, leaving behind the magnetic intensity in Fig. 3(b). A strong peak at $d = 3.43$ Å and broader intensity around $d = 3.04$ Å are present at 5 K. By 50 K, this intensity is diminished and changes shape around $d = 3.04$ Å, becoming more concentrated toward the center.

To identify the origin of the structural diffuse scattering, the intensity from an R/M random stacking model was simulated, and the results are shown in Figs. 4(a)–4(c). The simulated intensity was obtained from the squared structure factor of a supercell constructed with a random mixture of R- or M-type stacking. From the simulated nuclear structural intensity in Fig. 4(a), it is evident that R/M stacking disorder does, indeed, result in a broadening of the intensity within the $2.8 \leqslant d \leqslant 3.4$ Å range. (We show in the Supplemental Material, Sec. V [29], that although there are two R-type and three M-type stacking options, the specific types of M- or R-type stacking that are involved have only a subtle effect on the intensity.) In Figs. 4(b) and 4(c), we present two models for the magnetic scattering. The M-AFM model has flipped spins across every M-type stacking boundary [as depicted in Fig. 1(b)], and the M-FM model assumes all of the spins are aligned in the same direction regardless of stacking. A cursory comparison between the results of these two models and the magnetic intensity in Fig. 3(b) shows that the M-AFM model [Fig. 4(b)] has much better agreement with our data.

Strikingly, the M-AFM model predicts that the $(110)_R$ peak near $d = 3.43$ Å remains almost unchanged as R-type stacking is replaced with M-type stacking, with its d-spacing shifting by only -0.013 Å from $(110)_R$ to the corresponding $C2/m$ peak at $(11\frac{1}{2})_R$. (See Supplemental Material, Secs. V and VI, for a mathematical explanation [29].) In Fig. 3(g), we show the fitted position of this peak as a function of temperature, showing an abrupt shift above 50 K of about $+0.007$ Å. If we assume this change corresponds to a shift toward $(110)_R$ from $(11L)_R$, where L represents the average position of the peaks arising from a distribution of M-type stacking fractions, we obtain an estimate of 73(8)% M-type stacking, roughly consistent with our estimate of ~63% from the low-d refinement. [A slight increase in the width of the $(110)_R$ peak below ~53 K was reported in Ref. [40] and interpreted as evidence that the spin-spin correlation length was finite even at low temperature, but in light of our results, such a peak broadening is, instead, likely due to the presence of a distribution of M-type stacking fractions in the sample, resulting in a superposition of peaks at $(11L)_R$ with a range of L values within $-\frac{1}{2} \leqslant L \leqslant 0$.]

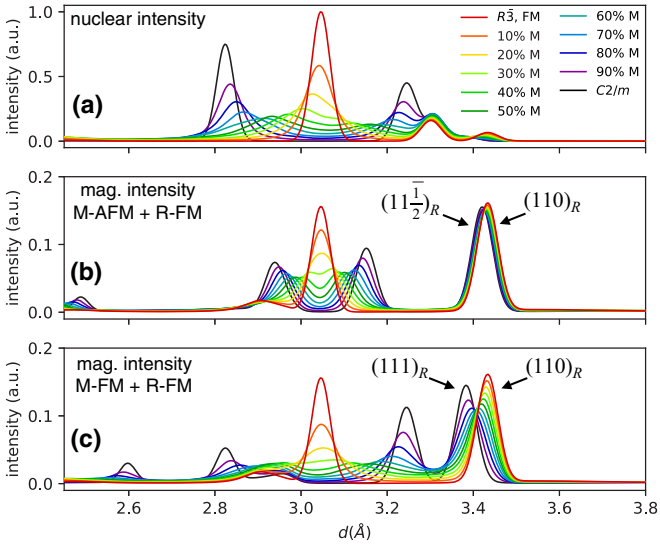

FIG. 4. Simulation of the (a) nuclear diffuse scattering intensity, and magnetic diffuse scattering intensity within the (b) M-AFM and (c) M-FM models for various percentages of M-type stacking.

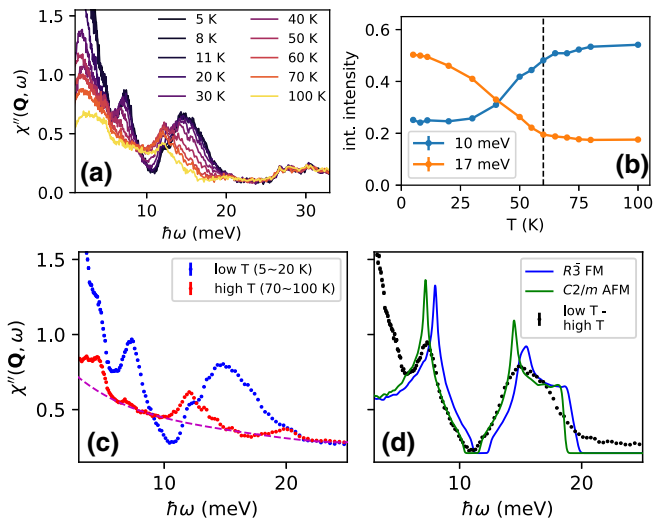

FIG. 5. (a) Inelastic neutron scattering intensity (Bose-factor corrected) as a function of energy transfer for temperatures taken on warming from 5 to 275 K along the low-Q trajectory of VISION. (b) Temperature dependence of inelastic intensity near 10 and 17 meV, averaged within ± 0.5 meV. The dashed line indicates 60 K. (c) Inelastic intensity (Bose-factor corrected) plotted vs energy transfer with averaging over two sets of data: "low T" (5, 8, 11, and 20 K) and "high T" (70, 75, 80, and 100 K). The dashed line is a polynomial background fit to the high-T data. (d) To account for phonon peaks, the high-T data (with the fitted background subtracted) were subtracted from the low-T data and plotted as the black points. Also shown are curves of simulated intensity for the "$R\bar{3}$, FM" model (calculated from the "J-DM" parameters in Ref. [41]) and for the "$C2/m$ AFM" model (same as "$R\bar{3}$, FM", except with summed interlayer interaction of $+0.073$ meV instead of -0.59 meV [41,43]). Error bars are omitted for (a), but uncertainty is commensurate with scatter; error bars are smaller than the marker size for [(b)–(d)].

If M-type stacking is associated with a transition at ~50 K, then we would expect intensity associated with M-type stacking to decrease on warming faster than for R-type stacking. This is exactly what is seen in Figs. 3(c)–3(e), which are plots of the temperature dependence of the intensity integrated within the d ranges indicated by the dashed lines in Fig. 3(b). From the simulated M-AFM magnetic intensity [Fig. 4(b)], it is clear that the intensity near $d = 3.04$ Å is disproportionately from R-type stacking, while the surrounding intensity near $d = 2.96$ Å and 3.12 Å is predominately from M-type stacking. The intensity at $d = 2.96$ Å and $d = 3.12$ Å shows transitions at or just above 50 K, while the intensity at $d = 3.04$ Å shows a transition at ~60 K. This change can also be seen in the 50–70 K data in Fig. 3(b), in which a peak near $d = 3.04$ Å is still present, but its two side peaks at 2.96 and 3.12 Å are absent. Meanwhile, the peak near $d = 3.43$ Å has contributions from both M- and R-type stacking, and its intensity thus shows an ultimate transition at the higher of the two transition temperatures, ~60 K [Fig. 3(f)]. Thus, our elastic neutron scattering data show that the magnetic coupling across M-type stacking boundaries arises below ~50 to 55 K.

B. Inelastic neutron scattering

Inelastic neutron scattering intensity is shown in Fig. 5(a). VISION collects inelastic data at fixed incident neutron energy along two sets of detector banks; we focus on the "low-Q" data set where the magnetic intensity is stronger. The spin-wave dispersion of CrI_3 resembles that of the electronic band structure of graphene, where acoustic and optic branches disperse along the in-plane directions and meet at Dirac points. The data indeed show acoustic- and optic-branch features at temperatures below ~60 K, similar to $CrCl_3$ data also taken on VISION [44]. The optic-branch hump is centered around 15 meV, separated from the acoustic branch by a Dirac gap around 10 to 11 meV. A peak at the acoustic-branch saddle point can be seen at 7.3 meV, while there is a lack of a clear optic-branch saddle-point peak, presumably due to broadening by interlayer interactions or mixed stacking. Below 4 meV, additional features are present at temperatures lower than 20 K, likely due to the magnetic impurity phase discussed above, but minimal change is observed above 4 meV in this temperature range. Spin waves would also arise from the Cr_2O_3 impurity phase, but the energy scale of the dispersion is higher, with maxima around 40 to 50 meV [45], and the intensity is expected to be temperature independent below ~100 K since $T_N = 308$ K for Cr_2O_3.

Little change is seen on warming (for $\hbar\omega \geqslant 4$ meV) until ~30 K, at which point magnon dampening is observed, with the magnetic intensity being replaced by a paramagnetic background. These changes continue until $T_C \approx 60$ K, as seen from the temperature dependence of the intensity near 10 and 17 meV (integrated within ± 0.5 meV) in Fig. 5(b). This temperature response is different from $CrCl_3$, where the spin-wave energy decreases continuously, even across the Néel transition [44]; this different behavior is likely due to the interlayer magnetic coupling being two orders of magnitude smaller in $CrCl_3$ [46] than in CrI_3 [41]. At 10 meV, the intensity increases as the spin-wave renormalization fills in this energy range. At 17 meV, at the upper part of the optic branch,

the intensity gradually decreases and levels off at 60 K. Since the observed spin waves arise from the sample as a whole (i.e., from regions with R-type as well as M-type stacking), the presence of the transition at ∼60 K is as expected.

Shown in Fig. 5(c) is the dynamic susceptibility where the data from 5 to 20 K were averaged together to improve the statistics (blue points). To remove the phonon contribution, data averaged from 70 to 100 K (red points), after having a polynomial background fitted (magenta line) and subtracted, were subtracted from the 5 to 20 K data, as shown in Fig. 5(d) (black points). (The polynomial-fitted background is likely due to paramagnetic diffuse scattering intensity from CrI_3, which is, thus, not present at low temperature.) Although the effect of stacking disorder will be considered below, there appears to be a gap around 11.0 meV that is roughly 1 meV wide.

The spin-wave intensity in Fig. 5(d) is shifted downward by just under 1 meV relative to the observed $R\bar{3}$-phase spin-wave energies, as represented by a calculation based on the "J-DM" model of Ref. [41], which we plot as "$R\bar{3}$, FM" (or as seen from a direct comparison of our data with those in Ref. [41]). The calculated intensity in Fig. 5(d) was obtained from a powder-averaged simulation in SPINW [47], then convoluted with a narrow energy resolution [48] and a broad Q resolution (assuming a FWHM spread in scattering angle of about 25°, or ∼0.5 $Å^{-1}$.) The "$R\bar{3}$, FM" model includes three in-plane exchange interactions, single-ion anisotropy, a Dzyaloshinskii-Moriya interaction, and two interlayer magnetic coupling constants for the first- and second-nearest-neighbor interlayer Cr-Cr bonds. We use this model as representative of $R\bar{3}$-phase spin-wave energies since it agrees well with the data [41,42], at least for the locations of the saddle-point peaks and Dirac gap, though the model does disagree in the higher-energy region (seen in powder data [42]), where it predicts a sharp drop off in intensity while the data show a gradual decrease. Regardless, it is clear that there is a significant difference between the spin-wave energies in our data and those observed for $R\bar{3}$, likely due to the prevalence of M-type stacking in our sample. A similar energy shift (∼0.5 meV) relative to $R\bar{3}$-phase expectations can be discerned in inelastic tunneling spectroscopy data on (presumably M-stacked) bilayer CrI_3 [49].

Interestingly, a ∼1 meV shift has also been observed in data on a powder CrI_3 sample that had been ball-milled overnight [42]. However the elastic intensity for that sample was largely featureless, lacking the clear peaks of our data in Fig. 3(a), suggesting that ball-milling overnight (rather than grinding for a few minutes in a mortar and pestle) led to a nearly amorphous crystal structure, well beyond the stacking disorder present in our sample. The inelastic features in our data are also much sharper than those observed for the ball-milled sample of Ref. [42], which were broadened well beyond resolution. Thus, unlike the nearly amorphous sample of Ref. [42], our sample should be representative of the effect of disordered M/R-type stacking.

The primary effect of changing the interlayer magnetic coupling is to apply an energy shift to the spin-wave intensity since the interlayer coupling is a small perturbation compared to intralayer interactions. We introduce the "$C2/m$, AFM" model, which has the same (intralayer) parameters as for "$R\bar{3}$, FM", except that the interlayer magnetic coupling, which sums to −0.59 meV per Cr^{3+} ion for the $R\bar{3}$ model, is replaced with an AFM interlayer exchange of 0.073 meV (i.e., 0.073/4 meV per nearest-neighbor interlayer bond in the $C2/m$ structure). The value of 0.073 meV is based on an analysis [41] of Raman spectroscopy data on bilayer CrI_3 [43]. Calculations for these models are shown in Fig. 5(d). The main difference between these models is an energy shift of ∼0.8 meV from $C2/m$ to $R\bar{3}$. The Dirac gap, in particular, remains largely unchanged. (We note that it is the *magnitude* of the interlayer coupling which determines the size of the energy shift since there is cancellation in simultaneously swapping the sign of the interlayer coupling constants and the directions of the spins.) The fact that our data in Fig. 5(d) line up almost exactly with our calculated $C2/m$ AFM-model curve would seem to imply that our sample is entirely M-type stacking (rather than our estimate of ∼63% M-type stacking), but we should remember that there is uncertainty in the intraplane interactions of the models that we have borrowed from (as is evident by the changes in refined exchange parameters in subsequent studies as better data were obtained [39–41]).

The effect of the M/R stacking disorder should be to narrow the gap somewhat (discussed in the Supplemental Material [29]), but the gap's presence in our data appears to be a natural consequence of the gap being the same size in the "$C2/m$, AFM" and "$R\bar{3}$, FM" models. Thus, assuming that the magnon gap in the $R\bar{3}$ phase is topological due to intraplane Dzyaloshinskii-Moriya interactions, as has been proposed [39,41], then a topological gap in the $C2/m$ phase (or in a mixed-stacking phase) should open for the same reason.

C. Magnetization measurements on a pressed pellet

The magnetization data also indicate a connection between stacking disorder and magnetic ordering. We performed magnetization measurements on a pressed pellet of ground CrI_3 powder, with the pressing presumed to preserve disordered M-type stacking down to low temperature. In Fig. 6(a), the magnetization M as a function of temperature T is shown, with its slope dM/dT plotted in Fig. 6(b). The sample was first cooled to 2 K, at which point a field of $\mu_0 H = +0.01$ T was applied, and zero-field-cooled (ZFC) data were collected on warming to 300 K. Field-cooled (FC) data were then collected on cooling back to 2 K. On warming, we see that the 0.01 T field is initially insufficient to reverse the sample's negative magnetization that happened to have set in on its first cooling. Above ∼50 K, however, the magnetization rises sharply and becomes positive. The AFM coupling across the M-type boundaries causes the spin direction to flip back and forth on crossing these boundaries, resulting in an almost random spontaneous magnetization in any given region, but above ∼50 K, the disappearance of the AFM coupling leaves disconnected FM R-type-stacked regions that are free to align in response to a small field. With higher temperature comes greater thermal fluctuations, and thus the magnetization in Fig. 6(a) drops on further warming, with FM order vanishing near the usual transition temperature of $T_C = 61$ K [11]. On cooling, the magnetization rises sharply below ∼60 K, but flattens just under 50 K before having an upturn on

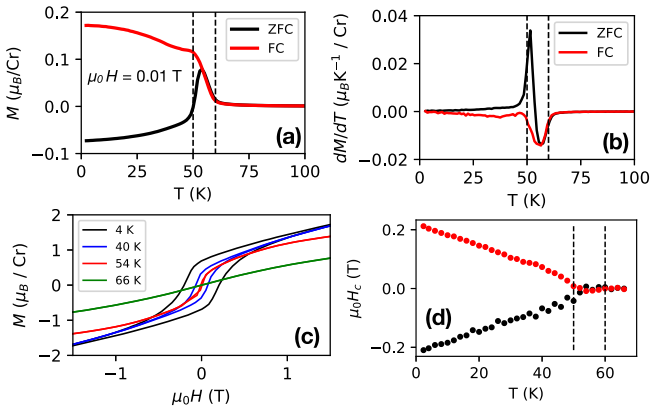

FIG. 6. (a) Magnetization vs temperature for a pressed pellet of CrI_3 on warming (ZFC) and cooling (FC), taken at $\mu_0 H = 0.01$ T. (b) Derivative dM/dT of the data in (a). (c) Magnetization-field hysteresis loops collected at several temperatures on a pellet of pressed CrI_3 powder. A hysteresis is present at 4 and 40 K, but is gone by 54 K. (d) The coercive field $\mu_0 H_c$ (the field at which $M = 0$) plotted as a function of temperature, extracted from magnetization-field hysteresis loops. The hysteresis disappears around 52 K. Error bars are omitted for clarity, but uncertainty is assumed to be commensurate with scatter.

further cooling, showing the resistance to full FM alignment induced by the AFM coupling of the M-type stacking. The magnetization reaches a level of $\sim$0.17 μ_B/Cr, comparable to values reported in the literature for single crystals with $\mu_0 H = 0.01$ T applied out of plane [11,35], though those studies report the magnetization approaching its maximum near 60 K rather than 50 K. (At much larger fields of ± 9 T, we observe full magnetic saturation near the $\pm 3\mu_B/Cr^{3+}$ ion; see the Supplemental Material, Sec. VIII [29].)

Perhaps the clearest magnetization signal of the AFM transition is the closing of the magnetization-field hysteresis loop above $\sim$50 K. These data are shown in Fig. 6(c) for selected temperatures, and the coercive field $\mu_0 H_c$ (i.e., $\mu_0 H$ where $M = 0$) is plotted in Fig. 6(d). Despite the presence of FM order up to $\sim$60 K, the hysteresis vanishes around 52 K, showing the role of the AFM coupling across M-type stacking boundaries in pinning the magnetization. Anomalies in magnetization vs temperature data on bulk crystals have been reported before [36,37,50], sometimes attributed to AFM ordering across M-type stacking, but usually with the assumption that the behavior is confined to surface layers [17]. An increase in the coercive field with decreasing crystal thickness was also reported [50], though not directly attributed to M-type stacking. However, here we report the disappearance of the magnetization-field hysteresis above $\sim$50 K, which makes clear the connection between the magnetic anomalies and the presence of AFM order across M-type stacking boundaries. The hysteresis may have practical applications (e.g., since mixed stacking evidently induces hysteresis, it may be a strategy for improving retentivity in data storage based on vdW-layered magnetic materials [51]), but the hysteresis also provides a convenient way to diagnose possible mixed magnetic ordering in other vdW-layered compounds where the type of magnetic order is correlated with stacking.

IV. DISCUSSION

The neutron scattering data show that at low temperature, there is AFM order in CrI_3 wherever M-type stacking is present. The link between AFM and M-type stacking is not limited to thin flakes or the surfaces of bulk crystals, and is likely the source of anomalies in magnetization data [50] and the secondary phase seen via muon spin rotation [37]. Our bulk magnetization measurements provide additional evidence for this connection. More generally, our results show that neutron scattering can uncover details about interlayer magnetism at the nanoscale.

Beyond CrI_3, the effects of mixed interlayer magnetic coupling may be seen in many other compounds. In $CrCl_3$, for instance, M-type stacking reportedly has a tenfold-greater interlayer AFM magnetic coupling than the usual R-type stacking [9], but the potential of mixed stacking as a source of certain magnetization anomalies seen at low magnetic field [52] has not been widely investigated. In $CrBr_3$, while the M $\rightarrow$ R structural transition is well above room temperature [53] and even few-layer flakes tend to be R stacked [54], a kink in magnetization data [55] suggests the possibility of AFM order across M-type boundaries in $CrBr_3$. $Cr_2Si_2Te_6$ and $Cr_2Ge_2Te_6$ have also been reported to have anomalies in their magnetization data, attributed to magnetic anisotropy [56], but the possibility of mixed stacking should not be discounted. $RuCl_3$ is another honeycomb-layered material that is structurally similar to the chromium trihalides; it also has multiple magnetic transitions associated with stacking defects [57] (e.g., deforming a crystal introduces a second magnetic transition [58]). Finally, $Fe_{5-x}GeTe_2$, with $T_C \approx 310$ K, also reportedly has changes in both magnetic order and layer stacking as a function of Co doping [59]. In these materials, if stacking disorder is present, an analysis of diffuse neutron scattering intensity (and a careful look at magnetization data) may elucidate the nature of the interlayer coupling and potentially expand our knowledge of the many kinds of interlayer magnetism that can be present in vdW-layered materials.

V. CONCLUSION

In conclusion, we have performed elastic and inelastic neutron scattering measurements on a ground-powder CrI_3 sample. An analysis of the nuclear and magnetic diffuse scattering allows us to conclude that AFM spin alignment occurs across M-type stacking defects at temperatures below $\sim$50 to 55 K, even as FM order persists up to $\sim$60 K. Inelastic measurements showed a $\lesssim 1$ meV decrease in spin-wave energy relative to a reported $R\bar{3}$-phase model, indicating that the magnitude of magnetic coupling across M-type boundaries is significantly less than across R-type boundaries.

ACKNOWLEDGMENTS

The authors would like to acknowledge discussions with Jeffrey Teo. The work at the University of Virginia is supported by the U.S. Department of Energy, Grant No. DE-FG02-01ER45927. The Spallation Neutron Source is a U.S. DOE Office of Science User Facility operated by Oak Ridge National Laboratory.

[1] M. N. Baibich, J. M. Broto, A. Fert, F. N. Van Dau, F. Petroff, P. Etienne, G. Creuzet, A. Friederich, and J. Chazelas, Giant magnetoresistance of (001)Fe/(001)Cr magnetic superlattices, Phys. Rev. Lett. **61**, 2472 (1988).

[2] G. Binasch, P. Grünberg, F. Saurenbach, and W. Zinn, Enhanced magnetoresistance in layered magnetic structures with antiferromagnetic interlayer exchange, Phys. Rev. B **39**, 4828 (1989).

[3] K. S. Novoselov, A. K. Geim, S. V. Morozov, D. Jiang, Y. Zhang, S. V. Dubonos, I. V. Grigorieva, and A. A. Firsov, Electric field effect in atomically thin carbon films, Science **306**, 666 (2004).

[4] Y. Cao, V. Fatemi, S. Fang, K. Watanabe, T. Taniguchi, E. Kaxiras, and P. Jarillo-Herrero, Unconventional superconductivity in magic-angle graphene superlattices, Nature (London) **556**, 43 (2018).

[5] Y. Sun, S.-C. Wu, M. N. Ali, C. Felser, and B. Yan, Prediction of Weyl semimetal in orthorhombic $MoTe_2$, Phys. Rev. B **92**, 161107(R) (2015).

[6] K. Deng, G. Wan, P. Deng, K. Zhang, S. Ding, E. Wang, M. Yan, H. Huang, H. Zhang, Z. Xu, J. Denlinger, A. Fedorov, H. Yang, W. Duan, H. Yao, Y. Wu, S. Fan, H. Zhang, X. Chen, and S. Zhou, Experimental observation of topological Fermi arcs in type-II Weyl semimetal $MoTe_2$, Nat. Phys. **12**, 1105 (2016).

[7] R. Noguchi, T. Takahashi, K. Kuroda, M. Ochi, T. Shirasawa, M. Sakano, C. Bareille, M. Nakayama, M. D. Watson, K. Yaji, A. Harasawa, H. Iwasawa, P. Dudin, T. K. Kim, M. Hoesch, V. Kandyba, A. Giampietri, A. Barinov, S. Shin, R. Arita *et al.*, A weak topological insulator state in quasi-one-dimensional bismuth iodide, Nature (London) **566**, 518 (2019).

[8] J. Huang, S. Li, C. Yoon, J. S. Oh, H. Wu, X. Liu, N. Dhale, Y.-F. Zhou, Y. Guo, Y. Zhang, M. Hashimoto, D. Lu, J. Denlinger, X. Wang, C. N. Lau, R. J. Birgeneau, F. Zhang, B. Lv, and M. Yi, Room-temperature topological phase transition in quasi-one-dimensional material Bi_4I_4, Phys. Rev. X **11**, 031042 (2021).

[9] D. R. Klein, D. MacNeill, Q. Song, D. T. Larson, S. Fang, M. Xu, R. A. Ribeiro, P. C. Canfield, E. Kaxiras, R. Comin, and P. Jarillo-Herrero, Enhancement of interlayer exchange in an ultrathin two-dimensional magnet, Nat. Phys. **15**, 1255 (2019).

[10] M. Serri, G. Cucinotta, L. Poggini, G. Serrano, P. Sainctavit, J. Strychalska-Nowak, A. Politano, F. Bonaccorso, A. Caneschi, R. J. Cava, R. Sessoli, L. Ottaviano, T. Klimczuk, V. Pellegrini, and M. Mannini, Enhancement of the magnetic coupling in exfoliated $CrCl_3$ crystals observed by low-temperature magnetic force microscopy and x-ray magnetic circular dichroism, Adv. Mater. **32**, 2000566 (2020).

[11] M. A. McGuire, H. Dixit, V. R. Cooper, and B. C. Sales, Coupling of crystal structure and magnetism in the layered, ferromagnetic insulator CrI_3, Chem. Mater. **27**, 612 (2015).

[12] B. Huang, G. Clark, E. Navarro-Moratalla, D. R. Klein, R. Cheng, K. L. Seyler, D. Zhong, E. Schmidgall, M. A. McGuire, D. H. Cobden, W. Yao, D. Xiao, P. Jarillo-Herrero, and X. Xu, Layer-dependent ferromagnetism in a van der Waals crystal down to the monolayer limit, Nature (London) **546**, 270 (2017).

[13] Z. Wang, I. Gutiérrez-Lezama, N. Ubrig, M. Kroner, M. Gibertini, T. Taniguchi, K. Watanabe, A. Imamoğlu, E. Giannini, and A. F. Morpurgo, Very large tunneling magnetoresistance in layered magnetic semiconductor CrI_3, Nat. Commun. **9**, 2516 (2018).

[14] S. Jiang, J. Shan, and K. F. Mak, Electric-field switching of two-dimensional van der Waals magnets, Nat. Mater. **17**, 406 (2018).

[15] T. Song, Z. Fei, M. Yankowitz, Z. Lin, Q. Jiang, K. Hwangbo, Q. Zhang, B. Sun, T. Taniguchi, K. Watanabe, M. A. McGuire, D. Graf, T. Cao, J.-H. Chu, D. H. Cobden, C. R. Dean, D. Xiao, and X. Xu, Switching 2D magnetic states via pressure tuning of layer stacking, Nat. Mater. **18**, 1298 (2019).

[16] T. Li, S. Jiang, N. Sivadas, Z. Wang, Y. Xu, D. Weber, J. E. Goldberger, K. Watanabe, T. Taniguchi, C. J. Fennie, K. F. Mak, and J. Shan, Pressure-controlled interlayer magnetism in atomically thin CrI_3, Nat. Mater. **18**, 1303 (2019).

[17] B. Niu, T. Su, B. A. Francisco, S. Ghosh, F. Kargar, X. Huang, M. Lohmann, J. Li, Y. Xu, T. Taniguchi, K. Watanabe, D. Wu, A. Balandin, J. Shi, and Y.-T. Cui, Coexistence of magnetic orders in two-dimensional magnet CrI_3, Nano Lett. **20**, 553 (2020).

[18] L. Thiel, Z. Wang, M. A. Tschudin, D. Rohner, I. Gutiérrez-Lezama, N. Ubrig, M. Gibertini, E. Giannini, A. F. Morpurgo, and P. Maletinsky, Probing magnetism in 2D materials at the nanoscale with single-spin microscopy, Science **364**, 973 (2019).

[19] T. Song, X. Cai, M. W.-Y. Tu, X. Zhang, B. Huang, N. P. Wilson, K. L. Seyler, L. Zhu, T. Taniguchi, K. Watanabe, M. A. McGuire, D. H. Cobden, D. Xiao, W. Yao, and X. Xu, Giant tunneling magnetoresistance in spin-filter van der Waals heterostructures, Science **360**, 1214 (2018).

[20] D. R. Klein, D. MacNeill, J. L. Lado, D. Soriano, E. Navarro-Moratalla, K. Watanabe, T. Taniguchi, S. Manni, P. Canfield, J. Fernández-Rossier, and P. Jarillo-Herrero, Probing magnetism in 2D van der Waals crystalline insulators via electron tunneling, Science **360**, 1218 (2018).

[21] H. H. Kim, B. Yang, T. Patel, F. Sfigakis, C. Li, S. Tian, H. Lei, and A. W. Tsen, One million percent tunnel magnetoresistance in a magnetic van der Waals heterostructure, Nano Lett. **18**, 4885 (2018).

[22] N. Ubrig, Z. Wang, J. Teyssier, T. Taniguchi, K. Watanabe, E. Giannini, A. F. Morpurgo, and M. Gibertini, Low-temperature monoclinic layer stacking in atomically thin CrI_3 crystals, 2D Mater. **7**, 015007 (2020).

[23] N. Sivadas, S. Okamoto, X. Xu, C. J. Fennie, and D. Xiao, Stacking-dependent magnetism in bilayer CrI_3, Nano Lett. **18**, 7658 (2018).

[24] D. Soriano, C. Cardoso, and J. Fernández-Rossier, Interplay between interlayer exchange and stacking in CrI_3 bilayers, Solid State Commun. **299**, 113662 (2019).

[25] P. Jiang, C. Wang, D. Chen, Z. Zhong, Z. Yuan, Z.-Y. Lu, and W. Ji, Stacking tunable interlayer magnetism in bilayer CrI_3, Phys. Rev. B **99**, 144401 (2019).

[26] S. W. Jang, M. Y. Jeong, H. Yoon, S. Ryee, and M. J. Han, Microscopic understanding of magnetic interactions in bilayer CrI_3, Phys. Rev. Mater. **3**, 031001(R) (2019).

[27] Z. Sun, Y. Yi, T. Song, G. Clark, B. Huang, Y. Shan, S. Wu, D. Huang, C. Gao, Z. Chen, M. McGuire, T. Cao, D. Xiao, W.-T. Liu, W. Yao, X. Xu, and S. Wu, Giant nonreciprocal second-harmonic generation from antiferromagnetic bilayer CrI_3, Nature (London) **572**, 497 (2019).

[28] S. Djurdjić-Mijin, A. Šolajić, J. Pešić, M. Šćepanović, Y. Liu, A. Baum, C. Petrovic, N. Lazarević, and Z. V. Popović, Lattice dynamics and phase transition in CrI_3 single crystals, Phys. Rev. B **98**, 104307 (2018).

[29] See Supplemental Material at http://link.aps.org/supplemental/10.1103/PhysRevB.109.024409 for single-crystal x-ray diffraction data, a discussion of the in-plane lattice constant, an estimate of the M-type stacking fraction from refinement, a discussion of the unknown magnetic impurity phase, mathematical details on the diffuse scattering calculations, more discussion on calculated inelastic intensity, and additional magnetization data. The Supplemental Material also contains Refs. [60–67].

[30] X. Guo, W. Jin, Z. Ye, G. Ye, H. Xie, B. Yang, H. H. Kim, S. Yan, Y. Fu, S. Tian, H. Lei, A. W. Tsen, K. Sun, J.-A. Yan, R. He, and L. Zhao, Structural monoclinicity and its coupling to layered magnetism in few-layer CrI_3, ACS Nano **15**, 10444 (2021).

[31] C. Cao, X. Liu, X. Ren, X. Zeng, K. Zhang, D. Sun, S. Zhou, Y. Wu, Y. Li, and J.-H. Chen, Barkhausen effect in the first order structural phase transition in type-II Weyl semimetal $MoTe_2$, 2D Mater. **5**, 044003 (2018).

[32] R. He, S. Zhong, H. H. Kim, G. Ye, Z. Ye, L. Winford, D. McHaffie, I. Rilak, F. Chen, X. Luo, Y. Sun, and A. W. Tsen, Dimensionality-driven orthorhombic $MoTe_2$ at room temperature, Phys. Rev. B **97**, 041410(R) (2018).

[33] S. Li, Z. Ye, X. Luo, G. Ye, H. H. Kim, B. Yang, S. Tian, C. Li, H. Lei, A. W. Tsen, K. Sun, R. He, and L. Zhao, Magnetic-field-induced quantum phase transitions in a van der Waals magnet, Phys. Rev. X **10**, 011075 (2020).

[34] T. Su, M. Lohmann, J. Li, Y. Xu, B. Niu, M. Alghamdi, H. Zhou, Y. Cui, R. Cheng, T. Taniguchi, K. Watanabe, and J. Shi, Current-induced CrI_3 surface spin-flop transition probed by proximity magnetoresistance in Pt, 2D Mater. **7**, 045006 (2020).

[35] Y. Liu and C. Petrovic, Anisotropic magnetocaloric effect in single crystals of CrI_3, Phys. Rev. B **97**, 174418 (2018).

[36] J. Arneth, M. Jonak, S. Spachmann, M. Abdel-Hafiez, Y. O. Kvashnin, and R. Klingeler, Uniaxial pressure effects in the two-dimensional van der Waals ferromagnet CrI_3, Phys. Rev. B **105**, L060404 (2022).

[37] J. Meseguer-Sánchez, C. Popescu, J. L. García-Muñoz, H. Luetkens, G. Taniashvili, E. Navarro-Moratalla, Z. Guguchia, and E. J. G. Santos, Coexistence of structural and magnetic phases in van der Waals magnet CrI_3, Nat. Commun. **12**, 6265 (2021).

[38] P. A. McClarty, Topological magnons: A review, Annu. Rev. Condens. Matter Phys. **13**, 171 (2022).

[39] L. Chen, J.-H. Chung, B. Gao, T. Chen, M. B. Stone, A. I. Kolesnikov, Q. Huang, and P. Dai, Topological spin excitations in honeycomb ferromagnet CrI_3, Phys. Rev. X **8**, 041028 (2018).

[40] L. Chen, J.-H. Chung, T. Chen, C. Duan, A. Schneidewind, I. Radelytskyi, D. J. Voneshen, R. A. Ewings, M. B. Stone, A. I. Kolesnikov, B. Winn, S. Chi, R. A. Mole, D. H. Yu, B. Gao, and P. Dai, Magnetic anisotropy in ferromagnetic CrI_3, Phys. Rev. B **101**, 134418 (2020).

[41] L. Chen, J.-H. Chung, M. B. Stone, A. I. Kolesnikov, B. Winn, V. O. Garlea, D. L. Abernathy, B. Gao, M. Augustin, E. J. G. Santos, and P. Dai, Magnetic field effect on topological spin excitations in CrI_3, Phys. Rev. X **11**, 031047 (2021).

[42] L. Chen, M. B. Stone, A. I. Kolesnikov, B. Winn, W. Shon, P. Dai, and J.-H. Chung, Massless Dirac magnons in the two dimensional van der Waals honeycomb magnet $CrCl_3$, 2D Mater. **9**, 015006 (2022).

[43] J. Cenker, B. Huang, N. Suri, P. Thijssen, A. Miller, T. Song, T. Taniguchi, K. Watanabe, M. A. McGuire, D. Xiao, and X. Xu, Direct observation of two-dimensional magnons in atomically thin CrI_3, Nat. Phys. **17**, 20 (2021).

[44] J. A. Schneeloch, Y. Tao, Y. Cheng, L. Daemen, G. Xu, Q. Zhang, and D. Louca, Gapless Dirac magnons in $CrCl_3$, npj Quantum Mater. **7**, 66 (2022).

[45] E. J. Samuelsen, M. T. Hutchings, and G. Shirane, Inelastic neutron scattering investigation of spin waves and magnetic interactions in Cr_2O_3, Physica **48**, 13 (1970).

[46] A. Narath and H. L. Davis, Spin-wave analysis of the sublattice magnetization behavior of antiferromagnetic and ferromagnetic $CrCl_3$, Phys. Rev. **137**, A163 (1965).

[47] S. Toth and B. Lake, Linear spin wave theory for single-Q incommensurate magnetic structures, J. Phys.: Condens. Matter **27**, 166002 (2015).

[48] P. A. Seeger, L. L. Daemen, and J. Z. Larese, Resolution of VISION, a crystal-analyzer spectrometer, Nucl. Instrum. Methods Phys. Res. Sec. A **604**, 719 (2009).

[49] H. H. Kim, B. Yang, S. Li, S. Jiang, C. Jin, Z. Tao, G. Nichols, F. Sfigakis, S. Zhong, C. Li, S. Tian, D. G. Cory, G.-X. Miao, J. Shan, K. F. Mak, H. Lei, K. Sun, L. Zhao, and A. W. Tsen, Evolution of interlayer and intralayer magnetism in three atomically thin chromium trihalides, Proc. Natl. Acad. Sci. USA **116**, 11131 (2019).

[50] Y. Liu, L. Wu, X. Tong, J. Li, J. Tao, Y. Zhu, and C. Petrovic, Thickness-dependent magnetic order in CrI_3 single crystals, Sci. Rep. **9**, 13599 (2019).

[51] C. Zhang, L. Wang, Y. Gu, X. Zhang, X. Xia, S. Jiang, L.-L. Huang, Y. Fu, C. Liu, J. Lin, X. Zou, H. Su, J.-W. Mei, and J.-F. Dai, Hard ferromagnetic behavior in atomically thin $CrSiTe_3$ flakes, Nanoscale **14**, 5851 (2022).

[52] N. Bykovetz, A. Hoser, and C. L. Lin, Critical region phase transitions in the quasi-2D magnet $CrCl_3$, AIP Adv. **9**, 035029 (2019).

[53] B. Morosin and A. Narath, X-ray diffraction and nuclear quadrupole resonance studies of chromium trichloride, J. Chem. Phys. **40**, 1958 (1964).

[54] X. Han, J.-Y. You, S. Wu, R. Li, Y. P. Feng, K. P. Loh, and X. Zhao, Atomically unveiling an atlas of polytypes in transition-metal trihalides, J. Am. Chem. Soc. **145**, 3624 (2023).

[55] J.-Q. Yan and M. A. McGuire, Self-selecting vapor growth of transition-metal-halide single crystals, Phys. Rev. Mater. **7**, 013401 (2023).

[56] Q. Xie, Y. Liu, M. Wu, H. Lu, W. Wang, L. He, and X. Wu, Two stage magnetization in van der Waals layered $CrXTe_3$ (X = Si, Ge) single crystals, Mater. Lett. **246**, 60 (2019).

[57] A. Loidl, P. Lunkenheimer, and V. Tsurkan, On the proximate Kitaev quantum-spin liquid α-$RuCl_3$: Thermodynamics, excitations and continua, J. Phys.: Condens. Matter **33**, 443004 (2021).

[58] H. B. Cao, A. Banerjee, J.-Q. Yan, C. A. Bridges, M. D. Lumsden, D. G. Mandrus, D. A. Tennant, B. C. Chakoumakos, and S. E. Nagler, Low-temperature crystal and magnetic structure of α-$RuCl_3$, Phys. Rev. B **93**, 134423 (2016).

[59] A. F. May, M.-H. Du, V. R. Cooper, and M. A. McGuire, Tuning magnetic order in the van der Waals metal Fe_5GeTe_2 by cobalt substitution, Phys. Rev. Mater. **4**, 074008 (2020).

[60] M. A. McGuire, G. Clark, S. KC, W. M. Chance, G. E. Jellison, V. R. Cooper, X. Xu, and B. C. Sales, Magnetic behavior and

spin-lattice coupling in cleavable van der Waals layered $CrCl_3$ crystals, Phys. Rev. Mater. **1**, 014001 (2017).

[61] D. P. Kozlenko, O. N. Lis, S. E. Kichanov, E. V. Lukin, N. M. Belozerova, and B. N. Savenko, Spin-induced negative thermal expansion and spin-phonon coupling in van der Waals material $CrBr_3$, npj Quantum Mater. **6**, 19 (2021).

[62] S. Liu, M.-Q. Long, and Y.-P. Wang, Negative thermal expansion of two-dimensional magnets, Appl. Phys. Lett. **120**, 072403 (2022).

[63] B. H. Toby and R. B. Von Dreele, GSAS-II: The genesis of a modern open-source all purpose crystallography software package, J. Appl. Cryst. **46**, 544 (2013).

[64] R. E. Newnham and Y. M. de Haan, Refinement of the alpha Al_2O_3, Ti_2O_3, V_2O_3 and Cr_2O_3 structures, Z. Kristallogr. Cryst. Mater. **117**, 235 (1962).

[65] A. H. Hill, A. Harrison, C. Dickinson, W. Zhou, and W. Kockelmann, Crystallographic and magnetic studies of mesoporous eskolaite, Cr_2O_3, Micropor. Mesopor. Mater. **130**, 280 (2010).

[66] W. Chen, Z. Sun, Z. Wang, L. Gu, X. Xu, S. Wu, and C. Gao, Direct observation of van der Waals stacking-dependent interlayer magnetism, Science **366**, 983 (2019).

[67] G. Shirane, S. M. Shapiro, and J. M. Tranquada, *Neutron Scattering with a Triple-Axis Spectrometer* (Cambridge University Press, Cambridge, UK, 2002).